Probing cosmic monsters: confronting hydrodynamic simulations with new observations of high-density environments

Ahad, S.L.

4

The intragroup light in KiDS+GAMA groups

Abstract

Galaxy groups and clusters assembled through dynamical interactions of smaller systems, resulting in the formation of a diffuse stellar halo known as the intragroup or intracluster light (IGL/ICL). By preserving the records of these interactions, this diffuse light provides valuable insight into the growth history of the halos and their brightest galaxies. Groups are especially interesting in this context because they represent the link between galactic haloes and massive clusters. However, low surface brightness makes it extremely challenging to detect their diffuse light individually. Recent deep wide-field imaging surveys allow us to push such measurements to lower brightness limits by stacking data for large ensembles of groups, which suppresses the noise and biases in the measurements. However, standard data processing pipelines for such surveys are not optimised to retain the diffuse light in IGL/ICL at extended radii. In this work, we present a special-purpose pipeline to reprocess individual KiDS exposures in $r-$band that optimises the IGL detection. Using an initial sample of 2385 groups with at least five spectroscopically-confirmed member galaxies from the Galaxy and Mass Assembly (GAMA) survey at $0.09 \leq z \leq 0.42$ and deep images from the Kilo-Degree Survey (KiDS, reprocessed with our updated pipeline), we present the first robust measurement of IGL from a large group sample down to 31-32 mag/arcsec^2 (varying in different stacked bins). We compare our stacked IGL measurements to predictions from matched mock observations from the Hydrangea cosmological hydrodynamic simulations. We find that systematics in the imaging data can affect IGL measurements even with our special-purpose pipeline. However, with a large sample and carefully optimised analysis, we can place well-constrained upper and lower limits on the IGL fraction for our group ensemble across redshifts $0.09 \leq z \leq 0.27$ and halo-masses $12.5 \leq \log_{10}[M_{200}/\mathrm{M}_\odot] \leq 14.0$ which are comparable to existing measurements of IGL in individual systems at similar redshift and halo mass range. This work explores the potential performance of statistical analysis of diffuse light in large samples of systems from next-generation observational programs like Euclid and LSST.

Ahad, S. L., Hoekstra, H., Bahé, Y. M., 2023, in preparation.

4.1 Introduction

It is well-established that the central galaxies (CG, also commonly referred to as the brightest group/cluster galaxy, BGG/BCG) in groups and clusters of galaxies are surrounded by an extended diffuse distribution of stars, which are often referred to as the intragroup or intracluster light (IGL/ICL, see e.g. Mihos, 2015; Montes, 2022, for recent reviews). Extending out to several hundreds of kilo-parsecs from the centre and often enveloping multiple galaxies in the host system, this diffuse light is generally considered as a separate component of the galaxy groups and clusters they are part of. Over the last few decades, different techniques have been explored to independently measure this diffuse component from their host system, especially to separate this from the CGs they surround. Depending on the measuring technique, the ICL has been found to contain as much as 30 per cent or more of the total starlight of the host system (e.g., Zibetti et al., 2005; Gonzalez et al., 2013; Mihos et al., 2017; Montes and Trujillo, 2018; Zhang et al., 2019; Kluge et al., 2021). However, a unanimous definition of this diffuse component (from simulations and observations) and how much they contribute to the total light of their host systems is still an open discussion (see, e.g. table 1 from Kluge et al., 2021). The origin and growth history of this diffuse light has been explored through multiple simulation-based studies (see, e.g. Mihos et al., 2017; Contini, 2021, for more discussion on the origin and growth of the ICL). These studies found several ways in which the IGL/ICL can build up, including tidal stripping (Gallagher and Ostriker, 1972), galaxy disruption (Guo et al., 2011), galaxy mergers (Murante et al., 2007), and in-situ star formation in the intracluster medium (Puchwein et al., 2010; Tonnesen and Bryan, 2012).

In recent years, studies on this diffuse light in individual clusters by using deep imaging have been increasing (e.g., Mihos et al., 2005; Montes and Trujillo, 2014, 2018; Jiménez-Teja et al., 2018; DeMaio et al., 2018, 2020; Montes et al., 2021), along with a few works where stacking a statistical sample of systems to improve the signal-to-noise-ratio have been performed (e.g., Zibetti et al., 2005; Zhang et al., 2019). Some recurring findings indicate that the ICL mass distribution follows the global dark matter (DM) distribution (e.g., Montes and Trujillo, 2019; Alonso Asensio et al., 2020, from observations and simulations, respectively), and that rather than with the CG, ICL profiles align more with the underlying cluster halo (Kluge et al., 2021). These findings collectively imply that the ICL growth is connected to the evolution of the CG (which are often large elliptical galaxies) in the host system, the baryon fraction of galaxy clusters, and the build-up of large-scale structures like galaxy clusters where

the giant galaxies (BCG) reside.

Although most studies on this diffuse light are based on clusters because the ICL is more prominent and clusters are preferentially targeted by deep surveys such as HFF (Lotz et al., 2017) or BUFFALO (Steinhardt et al., 2020), studying the diffuse light in groups (or IGL) is particularly interesting for several reasons. Firstly, they cover the intermediate halo mass regime of galaxy structures between galaxy-sized haloes and galaxy clusters. Therefore, understanding the build-up of the diffuse light corresponding to the halo mass of the system will not be possible without understanding the growth of IGL. Secondly, groups are interesting and distinct systems compared to the clusters because they are dynamically less disturbed, and have had fewer interactions with other systems. As a result, it is more straightforward to connect the growth of the IGL in groups with their dynamic history. Finally, according to the hierarchical structure formation model, the larger clusters are built by the infall and merging of smaller groups in their already existing larger haloes. In this scenario, a good fraction of the feedback and preprocessing of the member galaxies already happened in the groups before they even became part of a larger halo or a cluster. Detection of IGL at a $z = 1.85$ galaxy group by Coogan et al. (2023) supports this scenario. Recent works on detecting ICL in high-redshift clusters and protoclusters also provide evidence of the growth of this diffuse light for quite a long time over the age of the Universe (e.g. Joo and Jee, 2023; Werner et al., 2023). Therefore, understanding these smaller systems will lead to a better understanding of the physics of the larger systems.

Even though the importance of understanding the fractions and buildup of IGL/ICL across a wide range of host halo mass is clear, there have only been a few studies on IGL, and even fewer that cover a wide range of group-mass haloes so far. The main reason behind this is the lack of data with high enough resolution and signal-to-noise ratio (SNR) to reliably detect and analyze the faint IGL in groups.

Studying the light distribution of individual groups is useful to understand the diversity of the IGL signal and its formation channels. However, the low surface brightness of the IGL means that individual systems have a very low SNR, which makes the systematics in data to have a relatively more prominent effect on the measurements and introduces a higher uncertainty in their interpretations. Stacking the light of multiple groups can help to improve the SNR while keeping the key features of the underlying population. Zibetti et al. (2005) studied the diffuse light in 683 SDSS groups and clusters at $0.2 < z < 0.3$ using g, r, and i band photometry by stacking them to increase the SNR. They reported that, on average, the ICL contributes a small fraction ($\sim 10\%$) of the total visible light in a cluster. They also found that the surface

brightness of the ICL correlates with BCG luminosity and with cluster richness, but the fraction of the total light in the ICL does not vary notably with these properties. However, they only studied these behaviours by dividing their sample into two subsamples for each property (bright BCG - faint BCG, high richness - low richness) which may not be sensitive to a wider variation of these properties. With deep multi-band (u, g, r, i) photometry of the Kilo Degree Survey (KiDS, Kuijken et al., 2019) and the group catalogue based on spectroscopic redshifts by the Galaxy and Mass Assembly (GAMA, Driver et al., 2009; Driver et al., 2011) survey, we can now attempt to push the detection limit of the IGL and explore its co-evolution with the host systems across a wider halo mass range.

However, before simply stacking all the group data, we need to consider a few caveats. One important issue is the diversity of IGL/ICL distribution depending on the properties of the host system (groups/clusters) and its central galaxy (CG). Based on the data from their semi-analytic model, Contini and Gu (2021) reported that the ICL distribution varies widely depending on the dynamical history and morphology of the CG. Another recent work based on 170 low-redshift ($z \leq 0.08$) galaxy clusters in the northern hemisphere by Kluge et al. (2021) reported a positive correlation between CG+ICL brightness and different properties of the host cluster (e.g., mass, size, and integrated light in the satellites). Therefore, it is necessary to quantify the effect of galaxy and host system properties on the IGL measurements in a stacking analysis in order to find the optimal way of stacking for a reliable interpretation of the measurements. We explored this in Ahad et al. (2023), where we used mock observations of a GAMA-like group sample matching the KiDS $u-$ and $r-$band photometry using the Hydrangea cosmological simulations (Bahé et al., 2017). We utilise insights and predictions from Ahad et al. (2023) in this work to design and interpret our analysis.

Another major concern is the suitability of KiDS data for low-surface-brightness (LSB) analysis such as IGL measurement because of this being a cosmology survey with imaging from a wide-field camera. The data processing pipelines for cosmology surveys are usually optimised for measuring shapes and fluxes of small and faint galaxies. This requires a uniform photometric zero-point throughout the large joined pointings, which is often achieved by background-level detection and subtraction on very small scales compared to the total image size. The resulting images can have an uneven background, with the background over-subtracted near bright sources such as the CG of groups and clusters, making them quite unsuitable for IGL measurements. Moreover, in wide-field cameras like the OmegaCAM (Kuijken, 2011), the large aperture can cause internal reflection of light from bright sources, resulting in residual

(radial) patterns in the field image from uneven illumination. A wider field of view also increases the chance of streaks of diffused stray light from bright sources that are nearby, such as the Moon or planets. The stray-light and internal reflection issues are usually taken care of during the data processing phase. However, the standard corrections can leave extremely faint residual patterns in the field-of-view that only surface while stacking many images. This should be accounted for, especially in the case of an LSB analysis. Therefore, we develop a custom-made pipeline to re-process the KiDS data, taking special care of the background subtraction to retain a uniform background as much as possible.

In this paper, we present our custom pipeline to reprocess the multi-band (u, g, r, i) imaging from the KiDS data release 4 to optimise them for LSB analysis, and different checks that were done to ensure a robust measurement of the faint IGL in GAMA groups. We also present IGL measurements in stacked groups of different luminosities and redshift bins and compare them with predictions from the Hydrangea cosmological hydrodynamic simulations.

The organization of the paper is as follows. In Sec. 4.2, we present the GAMA groups and KiDS multi-band data we use for this work along with the selection criteria for our group sample. We also discuss the necessity of a custom pipeline for our analysis and describe the pipeline and its performance in keeping a uniform background level in the data in detail in this section (from Sec. 4.2.3 onward). In Sec. 4.3, we test the performance of the pipeline on retaining the diffuse light in galaxy outskirts and explore how to mask the diffuse light of satellite galaxies from the IGL measurements. In Sec. 4.4, we build an updated PSF model from the re-processed KiDS images and evaluate its impact on simulated IGL measurements. In Sec. 4.5, we present our resulting measurements and discuss how they compare to our predictions from simulations. Finally, in Sec. 4.6, we discuss the performance and expectation from wide-field surveys like KiDS in LSB analysis such as IGL measurement and summarise our findings.

4.2 Data

4.2.1 Galaxy and Mass Assembly survey data

The Galaxy And Mass Assembly (GAMA) project is a unique galaxy survey (Driver et al., 2009; Driver et al., 2011) with 21-band photometric data and spectroscopic redshifts of $\sim 300,000$ galaxies. The high completeness of the survey (98.5% complete

at $r-$band magnitude < 19.8 mag for SDSS-selected galaxies) allows for an excellent group selection (Robotham et al., 2011). The galaxy spectra in the GAMA survey were primarily measured by the AAOmega multi-object spectrograph on the Anglo-Australian Telescope in five fields covering a total of ~ 286 deg^2 area. As well as providing an almost volume-limited selection (of galaxies with $M_{\rm r} < 19.8$) at $z < 0.2$, the GAMA survey includes a large galaxy sample up to $z \sim 0.5$. Four of the GAMA fields (equatorial G09, G12 and G15 of 60 deg^2 each, and Southern G23 of ~ 51 deg^2) entirely overlap with the Kilo Degree Survey (KiDS, De Jong et al., 2013) – a large, deep, multi-band optical imaging survey that has great potential to reveal the faint IGL in GAMA groups (details in the following section).

We used the latest GAMA-II Galaxy Group Catalogue (`G$^3$CFoFv08`, Robotham et al., 2011) in this work. The catalogue was generated using a friends-of-friends (FoF) based grouping algorithm where galaxies are grouped based on their line-of-sight and projected physical separations. Information about the group member galaxies was obtained using an accompanying galaxy catalogue, `G$^3$CGalv09` (Liske et al., 2015).

To ensure the most robust group selection, we only considered groups with 5 or more member galaxies ($N_{\rm FoF} \geq 5$). After applying the $N_{\rm FoF}$ selection cut, we obtained a sample of 2389 groups. The distribution of redshift, CG magnitude, and halo mass of our final GAMA group sample is shown in Fig. 4.1. The halo masses were computed using the 'LumB' parameter of the `G$^3$CFoFv08` catalogue, and eqn. 37 of Viola et al. (2015). We used the stellar mass estimates and r-band magnitudes of GAMA galaxies from the `StellarMassesLambdarv20` catalogue (Taylor et al., 2011; Wright et al., 2016). This catalogue provides physical parameters based on stellar population fits to rest-frame $ugrizY$ spectral energy distributions (SEDs), and matched aperture photometry measurements of SDSS and VIKING photometry for all the $z < 0.65$ galaxies in the GAMA-II equatorial survey regions. This sample contains over 192,000 galaxies, and the stellar mass measurements assume $H_0 = 70$km s^{-1}Mpc^{-1}. Further details on the GAMA stellar mass derivation can be found in Taylor et al. (2011) and Wright et al. (2016).

4.2.2 Kilo Degree Survey

The Kilo-Degree Survey (KiDS, De Jong et al., 2013) is a large, deep, multi-band optical imaging survey that covers 1350 square degrees in four broadband filters (u, g, r, i). This cosmology survey was designed with the primary goal of mapping the large-scale matter distribution in the Universe and constraining the equation-of-state of dark en-

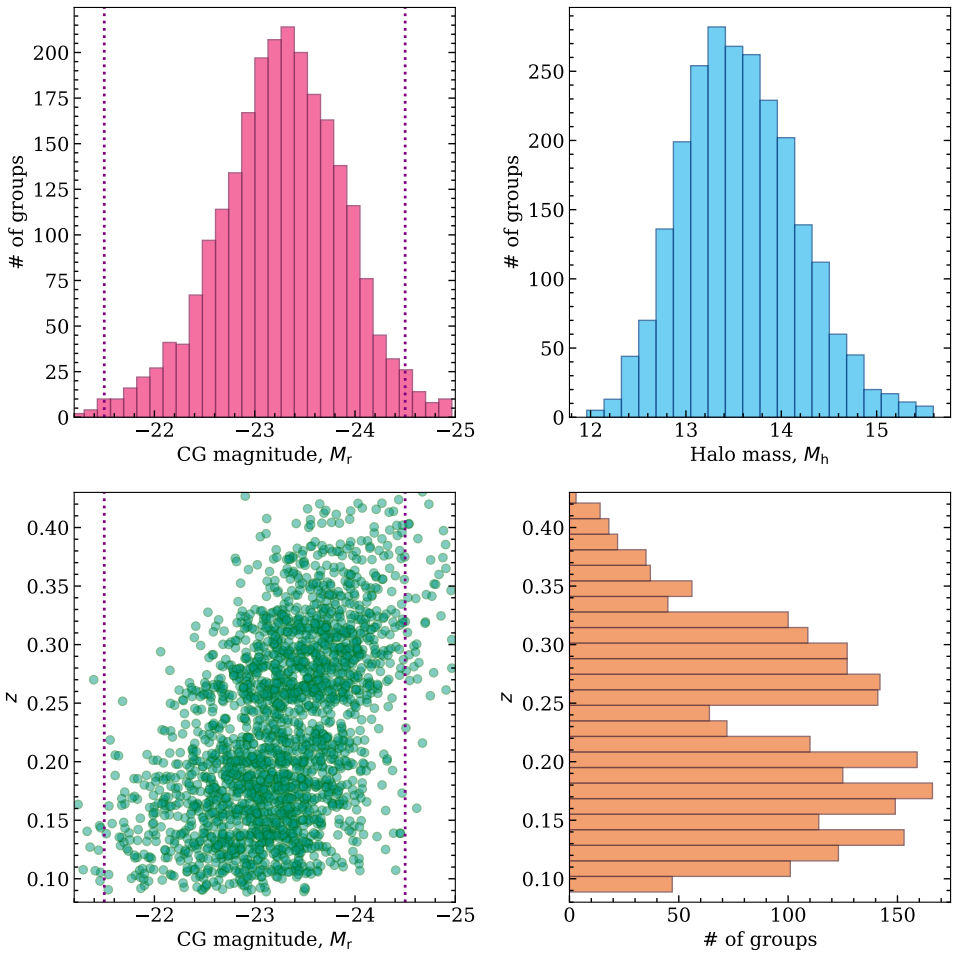

Figure 4.1: Distributions of different properties of the GAMA groups in our sample with $N_{\rm FoF} \geq 5$. The absolute $r-$band magnitudes (M_r) and redshifts (z) of the central galaxies (CG) were directly obtained from the GAMA-II Galaxy Group Catalogue (G^{3}CFoFv08, Robotham et al., 2011). The halo masses were computed from eqn. 37 of Viola et al. (2015). The vertical lines in the left panels indicate the magnitude range of the group CGs used in this work.

ergy (some recent results can be found in, e.g. Giblin et al., 2021; Li et al., 2023; Burger et al., 2023). The cosmological analysis includes measuring the effect of line-of-sight large-scale structures on galaxy shapes due to weak gravitational lensing. KiDS imaging was obtained with the square 268-million pixel CCD mosaic camera OmegaCAM (Kuijken, 2011) that covers a $1.013^\circ \times 1.020^\circ$ area at $0''.213$ pitch at the VLT Survey Telescope (VST; Capaccioli and Schipani, 2011; Capaccioli et al., 2012). The best seeing conditions (FWHM $< 0''.8$) were used for exposures in the $r-$band filter in order to take deep images (mean limiting $m_r = 25.02$ within 5σ in a $2''$ aperture) for the measurement of galaxy shapes. The GAMA group catalogue with spectroscopically confirmed member galaxies, accompanied by the deep KiDS imaging, provides us with a unique opportunity to analyze the IGL around the low-mass galaxy groups.

The optical imaging of the survey included in the public data release was produced by two dedicated pipelines. The AstroWISE information system (McFarland et al., 2013) was used for producing the co-added images in the *ugri* bands, and the THELI (Erben et al., 2005; Schirmer, 2013) pipeline was used to separately reduce the $r-$band images for providing a suitable source catalogue for the core weak lensing science case. These pipelines were optimized to have a uniform photometric zero-point throughout the full mosaic, which is essential for measuring shapes and photometry of small faint galaxies. However, the sky background is defined locally (by interpolating a 3×3 median-filtered map of background estimates in 128×128 pixel blocks), and can be over-estimated around bright sources (like central group/cluster galaxies) in the resulting images. Such background over-subtraction does not impact the galaxy shape measurements, however, it strongly affects the faint diffuse light around bright galaxies. The final outputs from the standard KiDS pipeline are therefore unsuitable for low-surface-brightness (LSB) analyses such as a measurement of the IGL, and require a re-processing of the raw images to retain the faint light. We explain the reasoning more in Sec. 4.2.3, and introduce our updated pipeline to reprocess the KiDS data for IGL analysis in Sec. 4.2.3 (also see Fig. 4.5 for the impact of the standard and updated pipeline on PSF profile). For further details on the latest (fourth) public data release of the KiDS survey, and the image reduction procedure, we refer the interested reader to Kuijken et al. (2019).

4.2.3 Customized data processing

Large cosmological imaging surveys, such as KiDS, aim to detect small, faint galaxies and measure their positions, fluxes, and shapes. Commonly, multiple exposures

(typically five in the case of KiDS) are combined to obtain a deeper image, which in turn is used for object detection. As the exposures are offset in position, and the background varies between them, an estimate for the background is subtracted before combining the data. This avoids imprinting the pattern of the individual chips in the final combined images used for object detection and photometry.

As the background also varies spatially, subtracting a constant value does not suffice. The standard KiDS pipeline uses SWARP (Bertin et al., 2002), which estimates the background on a mesh grid. The resulting values are clipped to remove outliers that may arise from the presence of bright stars. The mesh size sets the scale on which background variations can be captured, and it is typically chosen to be significantly smaller than the size of the chip, such that the spatial variations can be captured. A cubic spline is then fit through the remaining samples and this background model is subtracted. As cosmological applications focus on galaxies that are much smaller than the mesh size, this approach is adequate.

However, the presence of bright objects can bias the background estimate locally, thus leading to overestimating the background near those locations. As discussed in more detail in Sec. 4.4.1, this leads to a region of negative flux around bright stars. Similarly, we find that the surface brightness profiles of the group central galaxies are also affected. It may be possible to, at least partially, alleviate this problem by post-processing the survey images, as was done in Furnell et al., 2021. We take a different approach and reprocess the KiDS imaging data, attempting to take care to avoid this issue altogether.

For robust IGL measurements, we need to ensure that the background estimation is not correlated with the objects of interest. Provided the fact that we are averaging a large number of profiles, the impact of residual flux is to increase the uncertainty in the measurements. The residuals, which may be artefacts, scattered light from stars or galaxies below the detection limit, introduce excess variation in addition to the sky noise in the images. This is a major advantage of stacking the profiles of CGs, compared to analysing individual objects. In the latter, residuals may be difficult to distinguish from the signal of interest, whereas in a stacking analysis, residuals only contribute to a uniform background, albeit with increased noise. The only remaining concern is the contribution from satellite galaxies associated with the CGs, something we will explore in Sec. 4.3.2. We found that varying scattered light, in the end, is a limiting factor in these data.

Although we expect a stacking approach to be more robust, we nonetheless wish to reduce the contribution from residuals as much as possible, to ensure that they

are a subdominant contributor to the uncertainty in the measurements of the surface brightness profile. To this end, we developed an independent pipeline for the sole purpose of measuring the low surface brightness around bright galaxies in KiDS. In Sec. 4.2.3 we describe the various steps in the analysis and test the performance in Sec. 4.2.3. We demonstrate the value of our dedicated pipeline by measuring the average surface brightness profile around bright stars in Sec. 4.4.1.

Description of the pipeline

For our purpose, it is not necessary to combine the exposures of a pointing before measuring the profiles. Instead, we measure the profiles around the galaxies in each exposure and average these at a later stage. In principle, creating a catalogue with object detection from a stack would allow us to identify and mask fainter galaxies, but as the images are sky-background limited, we expect this to lead to a negligible improvement, while complicating the pipeline. We therefore process individual exposures in the various filters.

We start with the bias-subtracted and flat-fielded images ('reduced science frames') from the AstroWISE archive*. This ensures that the pixel response non-uniformities are accounted for. We want to ensure that we start with images with a minimal spatial variation in the sky level and with a minimum of coherent background features. To this end, we created a new flatfield from these science exposures. To do so, we first identified objects using SExtractor (Bertin and Arnouts, 1996) and masked those. The unmasked pixels were used to create the new flatfield that should, ideally, result in images with a constant background. However, this was unfortunately not the case.

The resulting flatfield for the r-band is shown in Fig. 4.2. The top image shows the full mosaic. We observe a clear radial pattern, which is caused by the illumination correction that is applied in the AstroWISE pipeline. The jumps between the chips arise because we normalise the individual chips to have a mean of unity. Unlike lensing studies that use these data to determine photometric redshifts, ensuring a consistent zero-point across the field-of-view is not essential for our aim: our objective is a smooth sky on average. To achieve this, we apply a zero-point correction to the background subtracted images, which is discussed in Sec. 4.2.3.

The bottom row in Fig. 4.2 shows the bottom-left chip, as well as a zoom-in of the top-left corner (red square). Although we started with already flat-fielded images, some structure is visible. This is likely caused by the variations in the illumination,

*http://www.astroWISE.org

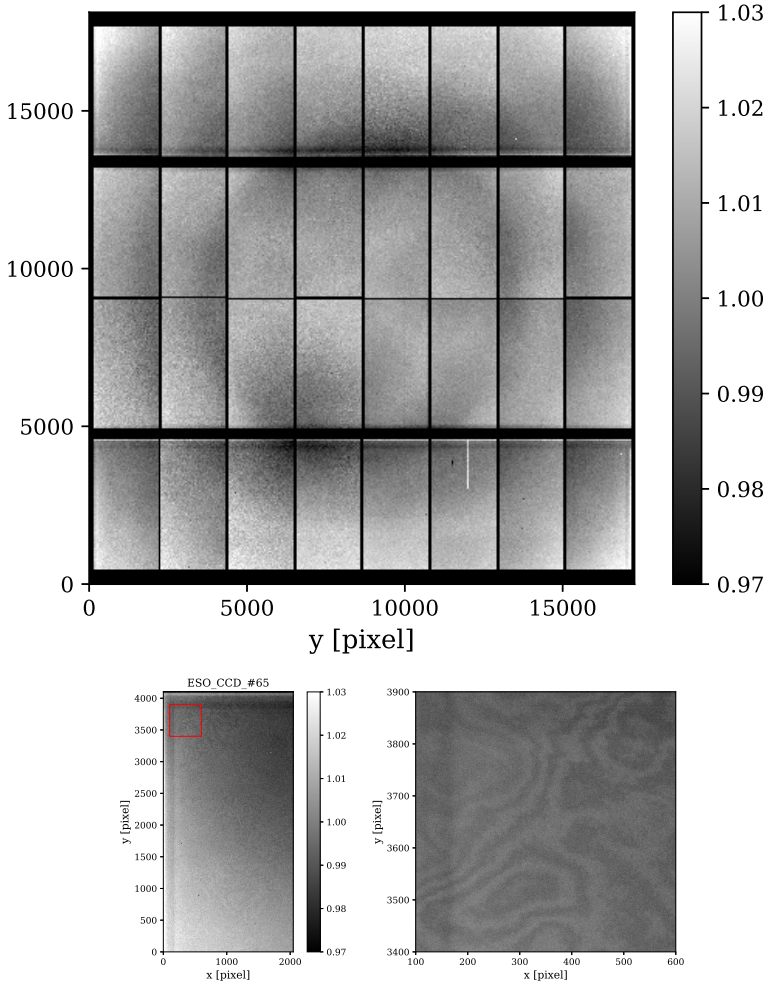

Figure 4.2: Flatfield in the r-band obtained by averaging the science observations that were already flatfielded using the standard AstroWISE pipeline. The top panel shows the full mosaic. The bottom figures show the bottom-left chip with a zoom-in of the top-left corner of that chip (red square). Some structure is visible, likely due to variations in the illumination, as well as some low-level fringing.

as well as some low-level fringing. Moreover, after we apply this additional flatfield to the data we find that the background also shows features. In particular, gradients in the background persist. The data we used in this paper were obtained early in the survey, as fields overlapping with GAMA were prioritized. At that time, the baffling of the telescope was not optimal (this was corrected later). This is the likely cause for the remaining variation, caused by changes in the illumination. We decided not to attempt further improvements and accepted that this will limit our IGL measurements in the end. To make the images more homogeneous for the masking step, we subtract a constant background from each chip using the median of the pixels that are unmasked in the SExtractor segmentation image.

Although the 'reduced science frames' contained an initial astrometric solution, it needed to be refined (in the standard KiDS pipeline, they were astrometrically calibrated at this stage as well). We used Scamp (Bertin, 2006) using the Gaia DR2 (Gaia Collaboration et al., 2018) as reference. To map the distortion of the camera we used a second-order polynomial because the overall distortion of the camera was found to be small. We found that with this setup the residuals in the astrometric solution are negligible (about $0\farcs01$ dispersion). We use Swarp without background subtraction to map the individual chips to a single image that is used for the measurements of the surface brightness profiles.

Internal reflections result in ghost haloes (for details on this feature and how they were masked, see de Jong et al. 2015). These are very apparent near bright stars, but are in fact always present. We chose to mask the reflection ghosts for very bright stars, for which the excess flux is clearly visible. This ensures that the most significant contributions are removed, while the remaining ghosts increase the uncertainty in our measurements somewhat. We determined the locations of the reflection ghosts as a function of position in the focal plane. We used the *Gaia* third Early Data Release (EDR3; Gaia Collaboration et al. 2021) to estimate the fluxes of bright stars in the images, and masked the affected regions if the predicted magnitude is brighter than $m = 10.5$ in the filter of interest. Although the ghosts are shaped like a doughnut, we also masked the inner regions. We also masked all stars brighter than $m = 16.5$ using the *Gaia* photometry with an aperture of radius $r_{\rm ap} = 175 - 20 \times (m - 10)$ pixels, which ensures that most of the starlight is masked.

We also masked bad columns. Finally, some of the images suffer from erratic gain variations caused by a problem with one of the video boards[†]. We identified those images and masked these from our analysis.

[†]http://www.eso.org/observing/dfo/quality/OMEGACAM/qc/problems.html

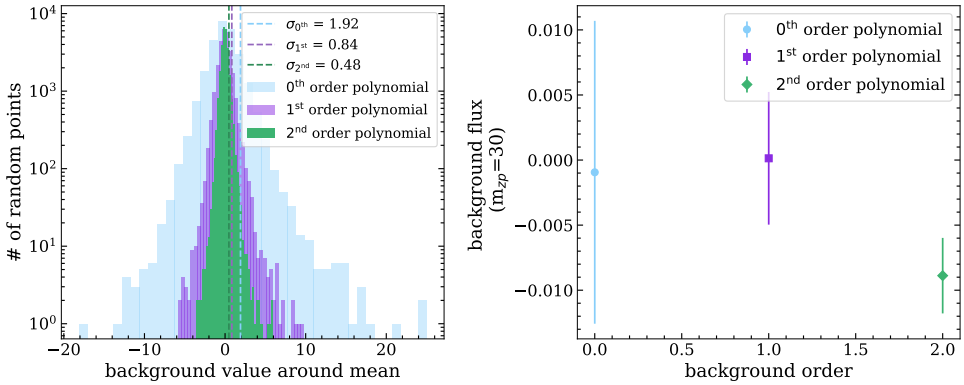

Figure 4.3: Left: histogram of the background values in randomly placed annuli on the field images with polynomial sky subtractions of order 0 (blue), 1 (purple), and 2 (green). The vertical lines denote the corresponding 1 σ values, as shown in the upper right corner. The scatter to the background values is smaller for higher-order polynomial estimation of the background. It is clear that higher-order polynomials remove spatial variation in the background more efficiently. Right: mean and scatter of the mean background values for the different polynomial background estimations (indicated in the upper right corner). This again demonstrates how the scatter is gradually reduced for higher-order polynomial estimation to the background values.

The contributions of remaining objects, stars, and galaxies were masked using the SExtractor segmentation images. We extend the marked regions in the segmentation image and explore the best setting in Sec. 4.3.2. The resulting masked images should only contain background, but occasionally objects are missed by SExtractor. These are readily removed by masking pixel values $|f| > 50$ counts (we adopt a zero-point where 1 count corresponds to $m = 30$). When measuring the surface brightness profiles around BGGs, we unmask the pixels that correspond to the segmentation image of the galaxy of interest.

Illumination and zero-point Correction

The non-uniform illumination due to the presence of additional stray light in the joined field images was corrected for all the photometric bands (for more details on the stray light issue, see de Jong et al. 2017 and Kuijken et al. 2019). For this, we selected SExtractor magnitudes (AUTO_MAG) of the stars with $m \geq 16$ in our field images and measured the residual systematic magnitude differences compared to the KiDS DR4 source catalogue (Kuijken et al., 2019), which was corrected for all these systematics. The spatial variations of these differences were then fitted with a second-

order, two-dimensional polynomial for a subset of the field images. As the distribution of the non-uniform illumination is expected to be the same for all the images in a particular filter for the same instrument, we took the average fitted coefficients for the two-dimensional polynomial and created a 'correction' image with the same pixel size of the field images. Each of the field images was then divided by the correction image on a pixel level to obtain the illumination-corrected images. As the background was already subtracted beforehand, this division does not affect the overall background level of the image, but makes the zero point of the sources spatially uniform. Using a second-order polynomial may leave some small-scale features in the photometric calibration, but this effect is mostly suppressed after stacking.

The zero-point shifts of all the illumination-corrected images were finally measured by comparing the magnitudes of the stars in each field to the KiDS DR4 source catalogue. These shifts were accounted for while converting counts to surface brightness of the CG radial profiles.

Performance of the sky subtraction

The masked images have a low background (we subtracted a constant value from each chip before combining them using SWARP), but now that most sources are masked, we need to improve the sky subtraction as there are still remaining gradients in the background. In this section, we explore the impact of subtracting a low-order polynomial from each chip.

To quantify the performance, we measured the scatter in the background estimates in randomly placed annuli with inner and outer radii of 100 and 150 arcseconds, respectively. We measured the mean and scatter in the values. Especially the latter is of interest, as a lower scatter implies we can measure the surface brightness profiles to larger radii. However, even though the images have been masked rather aggressively, the main concern is that the diffuse light around the CG may still impact the estimate. This will be more relevant for higher-order polynomial fits to the background. We therefore explore the impact on the galaxy profiles in Sect 4.3.1 as well because, in that case, the data are weighted differently. Nonetheless, focusing on the background estimates alone will provide a first indication of the performance of our pipeline.

Figure 4.3 shows the scatter of the background values in the randomly placed annuli described above for three different polynomial background estimations: zeroth order (blue), first order (purple), and second order (green) in the left panel. The right panel shows the mean values of the background with the standard error to the mean for each of the polynomial background estimations as indicated in the top right corner.

For each of the background estimations, 30 random annuli were placed in every field image and exposure. As all the SExtractor-detected sources, bad pixels containing too high or low values, and bright foreground stars were masked in the image before placing the random annuli (as described in sec. 4.2.3), some of the annuli had a large fraction of the possible pixels masked. Especially if the location of the annulus was near any of the bright stars, up to 90 per cent of the possible pixels in the annulus were masked in some cases. This gave rise to a higher noise and scatter to the mean background value for such annuli. To avoid such cases, we selected only those random annuli where at least 40 per cent of the total possible pixels in the annulus were unmasked for the background value estimation.

As is clearly visible from Fig. 4.3 (values of σ specified in the legend of the left panel and the error bars in the right panel), there is about a factor of two improvement in the scatter of the background values for each increased order of polynomial to subtract the background. This means that the precision of the background value estimation increases with increased order of the polynomial as structures in the background are removed, and for the cases we considered, a second-order polynomial results in the lowest scatter to the estimated value. However, to select the most efficient background estimation for our purpose, we also need to consider the accuracy of the background estimation. We explore this in Sec. 4.3.1.

4.3 Galaxy profiles

4.3.1 Impact of background subtraction on extended galaxy profiles

An over-subtracted sky background will particularly affect the outer edges of galaxy light profiles. If a model over-subtracts the background light, then the faint and diffuse light at the outer edge of a galaxy will be removed as background light. As a result, a galaxy's surface brightness (SB) profile will reach zero at a lower radial distance from the galactic centre, and the profile will have more negative values towards the outskirts. The background subtraction that preserves the most flux in the outermost radii of an extended source will therefore be the most accurate estimation of the global sky background. To test the accuracy of the background subtraction models, we checked the extended profiles of the bright sources with each of the background estimation cases (0^{th}, 1^{st}, and 2^{nd} order polynomials).

For this test, we selected GAMA groups at $0.09 < z < 0.15$ with a bright central

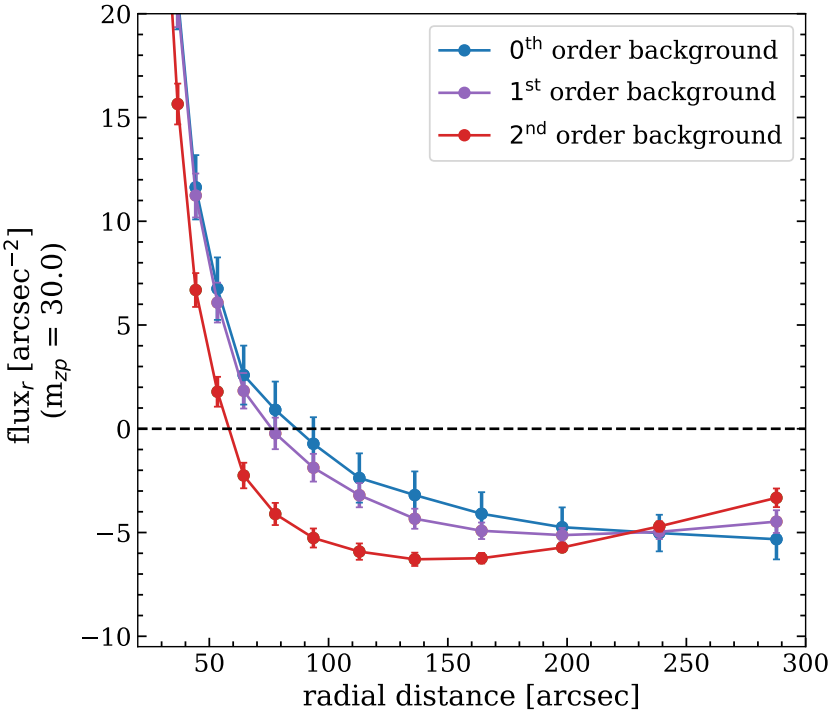

Figure 4.4: Surface brightness profiles of the group central galaxies beyond 20 arcseconds radial distance from the centre for 0^{th} (blue), 1^{st} (purple), and 2^{nd} (red) order polynomial background estimations, respectively. In all the profiles, error bars indicate 1σ uncertainties on the mean. All three profiles are the same within 20 arcseconds (not shown). Beyond that, however, higher-order background estimations over-subtract the background compared to the lower-order ones. This is the most prominent for the 2^{nd}-order polynomial estimation of the background.

galaxy ($M_r \leq -23$) and constructed their stacked SB profiles for each of our background models. The extended part of the resulting SB profiles is shown in Fig. 4.4. As visible from the figure, the 0^{th} order polynomial fit to the background retains the most light at the outer edge of the galaxies, with higher order polynomial fits retaining consecutively less light, and 2^{th} order fit having the worst case of light retention at the outskirts. Considering the tests demonstrated here and in Fig. 4.3, the 1^{st} order background subtraction seems to have a reasonable performance in both cases. However, none of the background subtraction models is unambiguously preferred above the rest. In our following analyses and tests, we therefore use all three background-subtracted images and compare their performances.

4.3.2 Masking the satellites

Along with the central galaxies, large satellite galaxies in galaxy groups and clusters can also have extended light, albeit a smaller amount. In a stacking analysis, such residual satellite light can result in a systematically higher diffuse light estimation than the actual amount. While measuring the IGL, it is therefore essential to ensure that light from satellite galaxies is completely masked out. We obtain the initial masking to the satellite galaxies and other sources in the image from the segmentation map of the SExtractor output. However, such masks can fail to include the fainter light distribution around the sources, which is more visible for the satellite galaxies and projected nearby galaxies along the line of sight. To address this, we extended the source masks obtained from the segmentation map. An increased mask size is expected to cover possible faint light surrounding the sources, but it also has a potential risk of masking the faint IGL signal and reducing the total light fraction in the IGL. We explored different levels of mask extension to identify an optimum extension for our analysis, and found that a radial extension of the mask of at least 10 pixels is needed to lower the contribution of extended light from satellites in the CG+IGL content. We therefore used this 10-pixel mask extension throughout this work where any masking was used. More details on this test are provided in Appendix 4.6.1.

4.4 Prediction from simulations

In Ahad et al. (2023), we prepared mock observations from the Hydrangea simulations (Bahé et al., 2017; Barnes et al., 2017), a suite of cosmological hydrodynamic zoom-in simulations of 24 massive galaxy clusters with virial mass between $10^{14.0}$ and $10^{15.4}$ $M_\odot$

at $z = 0$. Each of the zoom-in regions includes the large-scale surroundings of the clusters to ≥ 10 virial radii (r_{200c}) at $z = 0$, containing many group-mass haloes in addition to the central clusters. The simulations were run using the AGNdT9 calibration of the EAGLE galaxy formation and evolution code (Schaye et al., 2015). Different subgrid physics models were used to simulate astrophysical processes that originate below the resolution scale of the simulation, including star formation, star formation feedback, radiative cooling and heating, stellar evolution, black hole seeding, growth, and feedback. For details about the simulation model, hydrodynamics scheme, and comparison of the model to observed galaxy properties, see Schaye et al. (2015), Schaller et al. (2015), Crain et al. (2015), and Bahé et al. (2017) and references therein.

The group sample in Ahad et al. (2023) was chosen to be comparable to our baseline KiDS+GAMA group sample with $0.09 \leq z \leq 0.15$. The $u-$ and $r-$band mock observations were also made with comparable noise levels to the KiDS data. However, to make a better comparison to the KiDS+GAMA group analysis, we still need to account for the smearing by the point spread function (PSF) of the KiDS images (with updated background models) on the stacked SB profiles from Hydrangea groups because light from the central part is detected at large radii.

4.4.1 Point spread function

The PSF of updated KiDS images was constructed following a similar method as Montes et al. (2021) and Zhang et al. (2019)[‡]: we constructed the PSF by stitching profiles of bright and faint stars in different sections because very bright stars are saturated in the central region and light from the fainter stars at larger radii are not detectable with a high signal-to-noise ratio.

We started by running SExtractor (Bertin and Arnouts, 1996) on each of our updated KiDS field images to obtain the source catalogues. To determine which stars are suitable for which parts of the PSF we used the half-light radius ('FLUX_RADIUS') and the magnitude ('MAG_AUTO') parameters of the detected sources. We also used the stellarity index ('CLASS_STAR') provided by SExtractor to classify if an object is a star (1) or a galaxy (0). To select the unsaturated stars, we used all objects with CLASS STAR larger than 0.65 (arbitrarily chosen to maximise selected stars in the flux vs. half-light radius parameter space). The saturated stars were chosen only from their magnitude and size.

[‡]This part of the analysis was carried out by Stefan van der Jagt as a part of his second-year MSc research project, which was partially supervised by me.

Estimating core, intermediate, and outer parts

We divided the PSF into 4 sections: core, intermediate, outer 1, and outer 2. The half-light radius and the aperture magnitude were used carefully to select which stars construct which part of the PSF. The core section is constructed from the SB profile of bright unsaturated stars between magnitudes 16.5 and 18. Slightly brighter stars with saturated central regions but extended profiles out to larger radii were used for the intermediate part of the PSF. These stars for the intermediate profile had magnitudes between 14 and 15.5. The outer 1 and outer 2 sections consist of the brightest stars in the fields of view, with magnitudes between 12 and 14. We chose to divide the brightest stars into two samples to make a better transition from the outer 1 part to the intermediate part.

Stacking and Stitching different parts of the PSF

To estimate the PSF, we made cutout stamps of stars, stacked the images, and from the stacked images, calculated their radial SB profiles. The sizes of these stamps vary based on the part of the PSF the stars were used for. For the core part, we did not need a profile that extends to the full range of the PSF, and made 100×100 pixel stamps centred on the stars. For the intermediate stars, we made 500×500 pixel stamps; for the stars in the outer 1 region, we made 1000×1000 pixel stamps, and for the outer 2 region stars, these were 2000×2000 pixel stamps.

We used the segmentation map from SExtractor to exclude all other sources except for the central star in each stamp. To exclude light that is not masked away by the segmentation map, we also applied a $3-\sigma$ clipping method (excluding any pixel that has a value above or below $3-\sigma$ from the median pixel value in the masked image, where the masks also included the central stars). We also excluded all the stars from the sample that have a brighter star in the field of view. Another influence on the background of the KiDS field images is the large reflection ghost caused by large saturated stars. These ghosts cause the surface brightness to be elevated in certain parts of the PSF. This effect was tested, and all the fields with such ghosts were removed from the stack in the final PSF estimation.

The selected stamps were stacked, and the radial SB profiles of the stacked images were measured. Finally, the four partial profiles were stitched together. The stitching was done by selecting part of the profile before it drops discontinuously from the continuum and replacing it with the next region from there. The final stitched PSF profile is normalised by the total flux in the PSF. The final PSF profile is shown in

Fig. 4.5. Figure 4.5 also shows the PSF from the original KiDS DR4 field images. Comparing these two PSF profiles, it is clear that the updated background-subtracted images can detect PSF flux at larger distances compared to the images from the standard pipeline.

Effect of PSF on the outskirts of the galaxy profiles

The PSF of the instrument distributes the bright light at the core of stars and galaxies to the outer region. As a result, the diffuse light at the outskirts of bright group CGs may get excess contribution from the smearing of the central light. We tested the effect of PSF on the IGL measurement in two ways. First, we measured whether the fraction of light in IGL changes due to the PSF. Second, we tested whether the radial range of IGL detection is affected by the PSF.

To measure the effect of the PSF on the IGL fraction measurement, we took stacked SB profiles of Hydrangea groups at relevant bins of their $r-$band magnitudes from Ahad et al. (2023) and fitted a single de Vaucouleurs profile to the CG to separate the IGL. The fitting was done for both unconvolved and PSF-convolved SB profiles. The fraction of light in IGL ($f_{\rm IGL}$) from the PSF-convolved profiles were measured using the corresponding PSF-convolved total group light profiles. The $f_{\rm IGL}$ measurements are shown in Fig. 4.6 for both convolved (blue) and unconvolved (grey) cases, with errorbars showing the uncertainty to the measurements given the sample size. As is visible from Fig. 4.6, the values do not change much considering the error bars. However, for groups with a brighter CG, $f_{\rm IGL}$ seems to be slightly underestimated due to the effect of PSF.

The measurement of $f_{\rm IGL}$ was done until an SB limit of 32 mag/arcsec^2. Along with measuring $f_{\rm IGL}$, we also checked how the radial range of IGL is affected by the PSF convolution within the SB limit. For this, we measured the radial distance from the group centre within which 90 per cent of the IGL is enclosed (r_{90}). For the three magnitude bins we considered, r_{90} increased with CG magnitude. Compared to the unconvolved profiles, values for r_{90} were about 100kpc larger in the PSF-convolved profiles. For the convolved profiles, r_{90} for the three considered magnitude bins were about 260, 380, and 470 kpc. We used these radial distances as the predicted distance limit to which the fraction of light in IGL was measured in GAMA groups.

The key conclusion from this test is that the PSF does increase the radial IGL detection range. However, it does not increase the measured $f_{\rm IGL}$ because the same PSF effect is also present in the total group light. As a result, the impact of the PSF is not large for the CG magnitude range we consider, but we consider this effect in

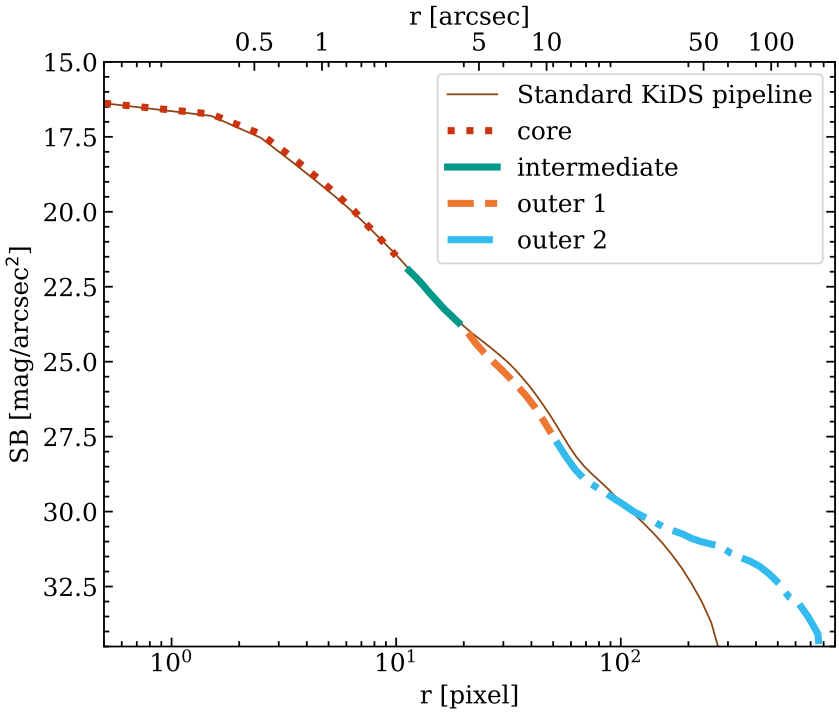

Figure 4.5: Stitched point spread function (PSF) from combining stars within different magnitude ranges (see text) from all fields with updated background-subtracted images. This PSF was re-normalized before convolving with the SB profiles of stacked Hydrangea groups. The colours and line styles indicate the radial range where different groups of stars (core, intermediate, outer 1, and outer 2) contributed to constructing the total PSF. The brown solid line shows the PSF constructed in the same way as above from standard KiDS data-release 4 images. The excess of faint light beyond 200 pixels in the PSF from the updated pipeline indicates the missing light in the standard KiDS pipeline.

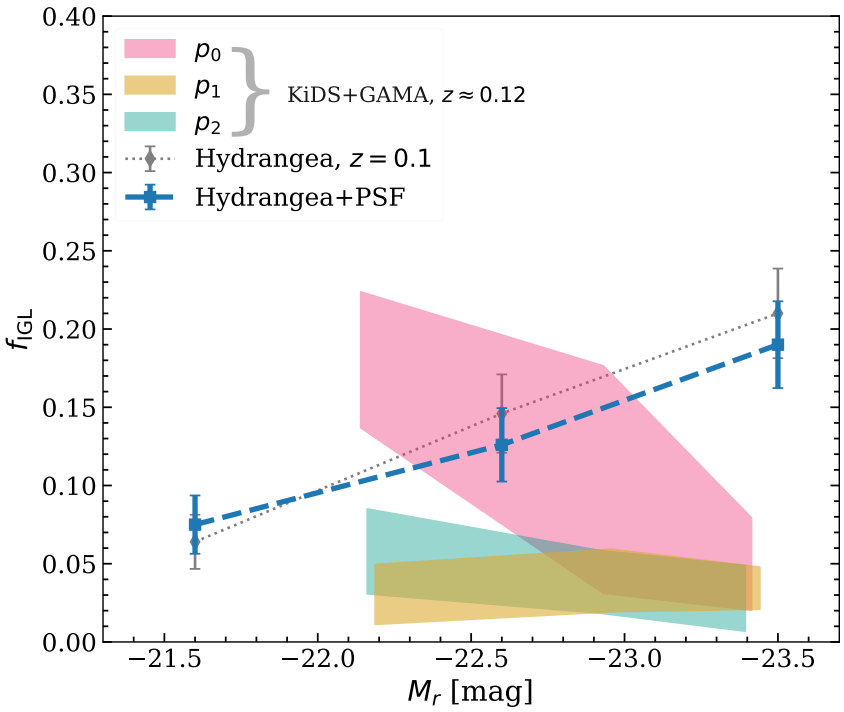

Figure 4.6: Fraction of light in IGL compared to the total group light ($f_{\rm IGL}$) of our KiDS+GAMA group sample at $0.09 < z < 0.15$ in the $M_{\rm r}$ bins they were stacked. The values along the x-axis indicate the mean $M_{\rm r}$ of the corresponding bins. Pink, yellow, and cyan shaded regions show the upper and lower limit of $f_{\rm IGL}$ for the 0^{th} (p_0), 1^{st} (p_1), and 2^{nd} (p_2) order background-subtracted images, respectively. Here, p_0 measurement is the upper limit of $f_{\rm IGL}$ for each magnitude bin at this redshift bin, while p_1 and p_2 measurements provide a lower limit. Details on how we define the upper and lower limits for each of the measurements are discussed in the text.

our comparison nevertheless.

4.5 The intragroup light in GAMA+KiDS groups

To quantify the intragroup light (IGL) in our group sample, we first measured the radial surface brightness (SB) profiles of each group from the reprocessed KiDS field images. The profiles were then checked visually to flag any profile that could potentially introduce bias in our measurements. Only the unflagged profiles were grouped in redshift and central galaxy (CG) magnitude bins before stacking and measuring the IGL in stacked profiles. Details of this process are given below.

4.5.1 Radial surface brightness profiles

For each of the KiDS pointings, we have five exposures in g, r, and $i-$bands and four exposures in $u-$band. Our results are based on the $r-$ band data because these are the deepest among the four bands. We did not create a mosaic of the pointings, but analysed each exposure separately. For each group, we created a 2×2 Mpc cutout (at the appropriate redshift) centred on the group CG.After applying the bright star and bad column masks, two different SB profiles were made from each cutout: (i) the CG+IGL SB profile that had all the sources masked except for the CG; and (ii) the total group SB profile that had all the sources masked, except for the group member galaxies (including the CG). The zero-point correction discussed in Sec. 4.2.3 was accounted for during the SB profile measurement.

During the total group light measurement, we applied an additional distance selection for the satellite galaxies considered for the total group light. This selection was made to account for the uncertainty in the group member assignment that comes from the aggregation of low-mass groups in the FoF halo finder algorithm. Jakobs et al. (2018) found that aggregation of multiple low-mass groups into one was present in 37 per cent of groups/clusters in their sample. To limit the inclusion of such wrongly-included satellite galaxies, we use the Rad_{50} and Rad_{100} parameters of the GAMA group catalogue, which indicate the distance from the group CG within which 50 and 100 per cent of the group members are located. Looking at the distribution of the $\mathrm{Rad}_{100}/\mathrm{Rad}_{50}$ ratio, we found that, in about 20 per cent of our group sample, there is at least one satellite galaxy that is more than $3\times\mathrm{Rad}_{50}$ away from the CG. We decided that these distant satellites are potentially wrongly-assigned group members due to the effect of aggregation and only considered satellites within $3\times\mathrm{Rad}_{50}$ distances from

the group CG in our total group light profiles.

4.5.2 Profile selection to lower measurement bias in stacking

During the stacking analysis, significant outliers can bias the overall measurement. Therefore, to ensure the robustness of our measurement, a representative subset of the SB profiles was visually inspected to identify possible causes for having an outlier and a 'flag' value was given to each of the SB profiles. A flag value of 0 indicates no issue and a good profile. A positive integer value of the flag was assigned based on the type of irregularity in the SB profiles. The most frequent reason to flag was the fraction of masked pixels in a cutout. If a group cutout or its central 25 per cent area had at least half of the total pixels in that area masked (bad pixels, stars, or other galaxies), it was flagged. If the masked fraction was low in a group, but the mask overlapped with part or entirety of the CG and resulted in a non-existent segmentation map at its CG location, it was also masked. If a CG SB profile had its brightest point shifted from the centre or had too low (≤ 200, compared to more than ~ 1000 for a standard profile) central flux count, it was also flagged. These particular cases happened mostly due to a partially masked CG, which was checked and confirmed for all the group cutouts that were assigned with the corresponding flag value. All of these flagging reasons are connected to our conservative masking procedure. In addition, SB profiles that had empty values (defined as 'not a number' or 'NaN', mainly in cutouts where masked areas covered a ring-like pattern around the CG for presence of many bright sources around) for multiple radial distances and CG+IGL SB profiles that had high scatter (larger than the median variation of flux count beyond 400 kpc for each considered group sample, usually ~ 1.0 flux count variation) in the far outskirts were also flagged. Finally, if any CG+IGL SB profile was flagged in ≥ 3 of the five available exposures, the rest were flagged for lack of reliability. After flagging, we were left with about 55 per cent of the initial SB profiles in each redshift bin we considered.

Another selection criterion we applied was removing GAMA groups that potentially have an ambiguous CG in the GAMA catalogue. In Ahad et al. (2023), we demonstrated that if the group CGs were selected based on the galaxy halo mass instead of selecting the brightest galaxy at the centre of light distribution, about 20 per cent of the GAMA groups in our sample gets assigned with a different CG (predominantly a red one instead of a blue one). We also showed in Ahad et al. (2023), based on our mock observations from Hydrangea simulations, that such miscentring can slightly suppress the IGL measurements. However, the small suppression is inferred from a

simulated sample-based work, in which case, we had information about the 'true' halo centre, which is not the case for observational data. Therefore, we chose only the GAMA groups in our sample that did not have a re-assignment of their CG based on the galaxy halo mass. This selection lowered our sample size by a further 10 per cent.

4.5.3 Sub-stacking based on BGG luminosity

In Ahad et al. (2023), we have found that, based on mock images of groups in the Hydrangea simulations, the IGL content has a positive correlation with the luminosity of the group CG. We also found that while stacking multiple group CGs, binning them along the absolute magnitude of the CGs preserved the underlying IGL fraction trend (fig. 8 of Ahad et al., 2023). We utilised this result in this work and stacked group CGs of similar absolute magnitudes.

To keep a uniform range of absolute $r-$band magnitude ($M_{\rm r}$) in our different redshift samples, groups with CG $M_{\rm r}$ between -21.5 and -23.5 were divided into three bins. The bin widths were selected to have a similar number of groups in each bin. The SB profiles of the groups in each redshift and magnitude bin were first normalised to have appropriate flux values at the mean redshift of the sample. Also, the radii in each bin were converted to physical kpc at their corresponding redshifts. Finally, the profiles were stacked to obtain the mean profile in each redshift and magnitude bin for the CG+IGL and total group light.

4.5.4 Residual background subtraction

Instead of a local background-subtraction in the standard AstroWISE pipeline, our approach of a chip-by-chip global background subtraction minimizes any remaining flux pattern in the background (e.g. as shown in Fig. 4.2). However, as Fig. 4.2 shows, there are also some small-scale patterns at the chip edges that are difficult to remove even with our updated background subtraction model. Besides, due to the presence of stray light (e.g., from the reflected light of planets), there are some global remaining patterns in the joined field image. These patterns result in a non-flat background in the field image, which is likely comparable in all the field images. We accounted for this residual background by measuring a background SB profile and subtracting this from the stacked SB profiles of groups.

To do so, we measured the residual background profile at a random location for each of the group profiles. The random locations were obtained by taking the pixel location of a group CG in one pointing and measuring SB profiles at the same pixel location and

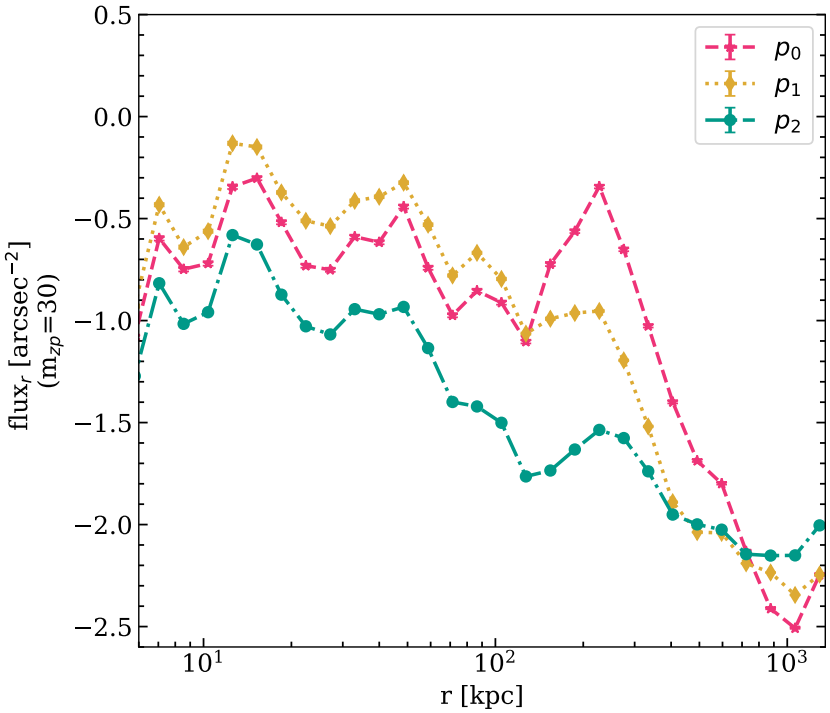

Figure 4.7: Surface brightness profile of the mean residual background at random points for the three background-subtracted field images used in this work. From the central region out to 100 kpc, their variation is similar. However, beyond 200 kpc, the 0^{th} order background-subtracted images (p_0) have a steeper downturn than the other two.

cutout size in a different pointing. While preparing these profiles, all the SExtractor detected sources were masked with extended segmentation maps, and the masking was similar to how the group profiles were made. No pointing-and-exposure combination was used more than once to create the background profiles. Because we use the pixel location and cutout size of a group to create the background SB profiles, any global background pattern that may be included in the group SB profile due to its location (e.g., the centre of the image or edge of a chip), is accounted for in the residual background profile. Finally, the background profile fluxes were adjusted for the zero-point correction, and the radial range was adjusted to the appropriate physical kpc units before stacking and subtracting them from the group SB profiles.

Figure 4.7 shows the mean residual background profiles in the field images for the three different background-subtraction models. Beyond 200 kpc, all the profiles shown have a downturn towards the end, especially for the 0^{th} (p_0) and 1^{st} (p_1) order background-subtracted images. This bias towards lower values in the outskirts is not as prominent for p_2 images. However, there is an overall trend of smaller values in the outskirts for the p_2 background profile. After subtracting this residual background profile, we could reach 32 mag/arcsec^2 SB limit for some of the stacked group profiles. In other cases, it was between 30 and 31 mag/arcsec^2.

4.5.5 Fraction of light in IGL

The fraction of light in IGL compared to the total group light ($f_{\rm IGL}$) in each redshift and magnitude bin was measured in a similar process as done in Ahad et al. (2023) using a single de Vaucouleurs (SD) profile fitting to keep the comparison consistent. We used the following steps:

1. Any residual flat background light at the far outskirts (beyond 500 kpc from the group centre) was removed by fitting a constant background to the outer profile.

2. The CG profile was fitted using a single de Vaucouleurs (SD) profile out to 40kpc from the CG centre. During this fitting procedure, the central 2.5 kpc region was not included to avoid any saturated pixels.

3. The fitted CG profile was subtracted from the CG+IGL profile to obtain the IGL profile. Any remaining light in the central region due to fitting beyond 2.5 kpc was excluded.

4. The total flux in the IGL was computed by integrating the IGL profile out to r_{90} for each magnitude bin based on the Hydrangea stacked profiles (see Sec. 4.4.1).

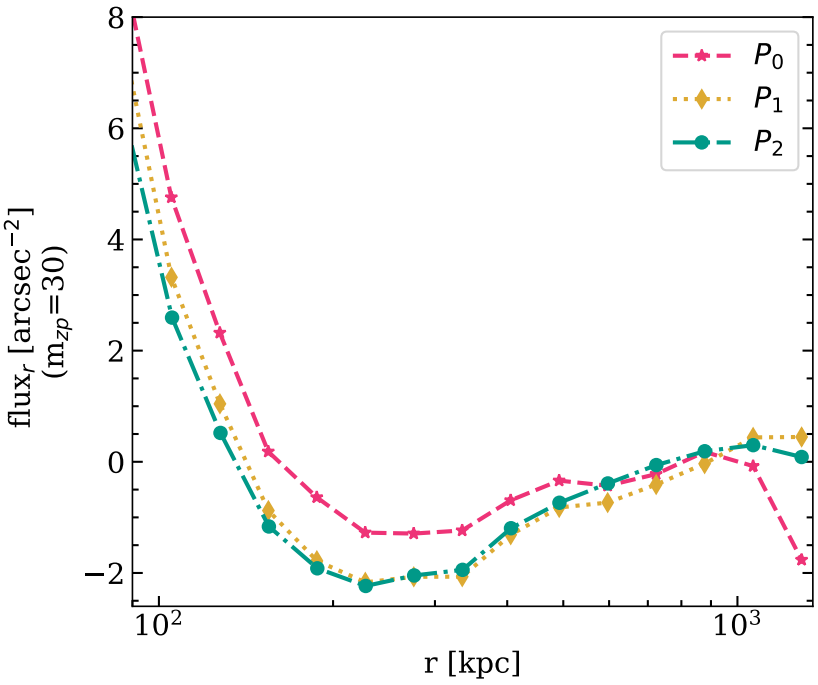

Figure 4.8: Surface brightness profile of the mean residual background at random points for the three background-subtracted field images used in this work. From the central region out to 100 kpc (not shown here), their variation is similar. However, beyond 200 kpc, the 0^{th} order background-subtracted images (p_0) have a steeper downturn than the other two.

Similarly, the total group light was measured by integrating the total group profile out to the same radial distance. Their ratio was taken as the fraction of total light in IGL, or $f_{\rm IGL}$.

The measured $f_{\rm IGL}$ in the redshift range $0.09 \leq z \leq 0.15$ with respect to the $M_{\rm r}$ bins in our three different background (p_0, p_1, p_2) subtracted images are shown in Fig. 4.6. The shaded regions in pink, yellow, and cyan are showing the upper and lower limits of $f_{\rm IGL}$ measurements for p_0, p_1, and p_2 cases, respectively. The blue dashed line here shows prediction from the Hydrangea simulations (details in Sec. 4.4). While our measurements for p_1 and p_2 background subtraction models are lower than the simulation predictions, $f_{\rm IGL}$ for the p_0 case is comparable to the predictions.

To define the upper and lower limit of $f_{\rm IGL}$ measurement for each background subtraction case for a specific redshift and magnitude bin (i.e. each of the shaded

regions), we considered the outer regions ($\leq$ 200 kpc) of the SB profiles. Figure 4.8 shows the outer regions for all three background subtraction cases at $0.09 \leq z \leq 0.15$ for the brightest magnitude bin we considered (mean $M_{\rm r} \approx -23.4$). We expect that the overall sky background dominates only beyond 500kpc from the group centres because most of the groups have a virial radius below this limit, and we see that the average flux count beyond this limit is consistent with 0 for all p_0, p_1, and p_2 cases. However, between 150 and 500 kpc distances from the group centres, all three profiles show a 'U' shaped down and up turn in the profile, which indicates a ring-like over-subtracted region in the image. This over-subtraction is similar for p_1 and p_2, which show a stronger over-subtraction compared to p_0. As there is no reliable way to recover this missing light, it poses a limiting factor in our measurements. For each of the p_0, p_1, and p_2 cases, we fitted a horizontal line to the data points beyond 500 kpc in Fig. 4.8 and considering it as the sky background, subtracted this value from these profiles before fitting the CG to separate the IGL. Given the over-subtracted region in the profiles, this background subtraction brings the extent of the SB profiles down to $\approx$ 190 kpc for p_0, and $\approx$ 150 kpc for p_1 and P_2. The IGL measurement from this background definition provided our lower limit to $f_{\rm IGL}$, which is shown in the lower bound of the shaded regions in Fig. 4.6 and Fig. 4.9. The upper limit to the measurements came from taking the minimum value of the profiles as the background value and subtracting that before the IGL measurement. In this case, all the profiles could be measured until the r_{90} limits defined in Sec. 4.4.1. This measurement and its scatter define the upper bounds of the shaded regions in Fig. 4.6 (and also Fig. 4.9 below).

Measurements with different background-subtraction models

Considering how we already showed in Sec. 4.3.1 that the p_0 model has the best retention of faint light at the outskirts of the galaxy SB profiles, we conclude that our measured $f_{\rm IGL}$ for p_0 (pink shaded region) is the upper bound of this measurement in all the background subtraction models we considered in this work. One point of concern here is that the p_0 model only subtracts a constant background, and therefore can leave the most amount of residual background pattern out of the three models we used. This can especially impact the $f_{\rm IGL}$ measurement for the fainter $M_{\rm r}$ bin, causing a potential overestimation. On a different note, the $f_{\rm IGL}$ measurement for the brightest $M_{\rm r}$ bin is likely the best estimate out of the three background subtraction models, although even p_0 shows signs of some over-subtraction at the edge of the SB profile of the brightest CGs (Fig. 4.8). Unlike p_0, both p_1 and p_2 profiles have

comparably high over-subtraction at the edge of the SB profiles (Fig. 4.8) and similar $f_{\rm IGL}$ measurements (Fig. 4.6). Considering all the above points, we decided to use only the p_0 background subtracted images to measure $f_{\rm IGL}$ in GAMA groups at different redshift ranges.

Impact of redshift on background and measurements

Groups with the same physical size have a smaller angular size at higher redshifts. Also, for the same apparent magnitude limit of the GAMA galaxy measurements, groups with intrinsically brighter CG are more numerous at higher redshifts. Compared to the groups with similarly luminous CGs at lower redshifts, these high redshift groups have different systematics in the data due to their different angular sizes on the sky. We check the impact of these different systematics on the $f_{\rm IGL}$ measurements in three different redshift bins. The first is our nearest redshift bin, $0.09 \leq z \leq 0.15$ (with and average $z \approx 0.12$), for which the $f_{\rm IGL}$ is shown in Fig. 4.6. The other two consecutive redshift ranges are $0.16 \leq z \leq 0.21$ (with an average $z \approx 0.18$) and $0.21 \leq z \leq 0.27$ (with an average $z \approx 0.24$). The $f_{\rm IGL}$ in these redshift ranges for the 0^{th} order background subtracted images (p_0) are shown in Fig. 4.9. The shaded regions show the upper and lower limits of $f_{\rm IGL}$ at different redshift ranges as indicated in the labels (how we define these limits is discussed previously in this section). Blue and purple lines indicate our predictions from Hydrangea simulations at comparable redshifts. The mean halo mass of the stacked groups in each bin is shown along the x-axis.

As is visible from Fig. 4.9, there is no strong redshift-evolution in the $f_{\rm IGL}$ measurements in either simulations or observations. Especially the measurements for the lowest-mass bins have similar values throughout. The measurements for the highest-mass bins slightly increase at higher redshifts, and their scatter gets smaller (as indicated by the vertical span of the shaded region). However, these increased $f_{\rm IGL}$ values are likely not an indication of increased IGL at these slightly higher redshifts, but an improvement of the profile over-subtraction issue at extended radial distances. Because our measurements are done on cutouts extending to 1 Mpc distance from the group centres, and this distance corresponds to less than half of the angular size at $z \approx 0.24$ compared to $z \approx 0.12$, the residual background patterns have a smaller impact on the group SB profiles. For example, a 1 Mpc cutout can span up to 6 CCD chips in the joined field of view at $z \approx 0.12$, including the uneven background at the chip edges. Compared to that, at $z \approx 0.24$, a 1 Mpc cutout can span only two chips, avoiding the large-scale residual patterns. Also, CGs with the same luminosity are

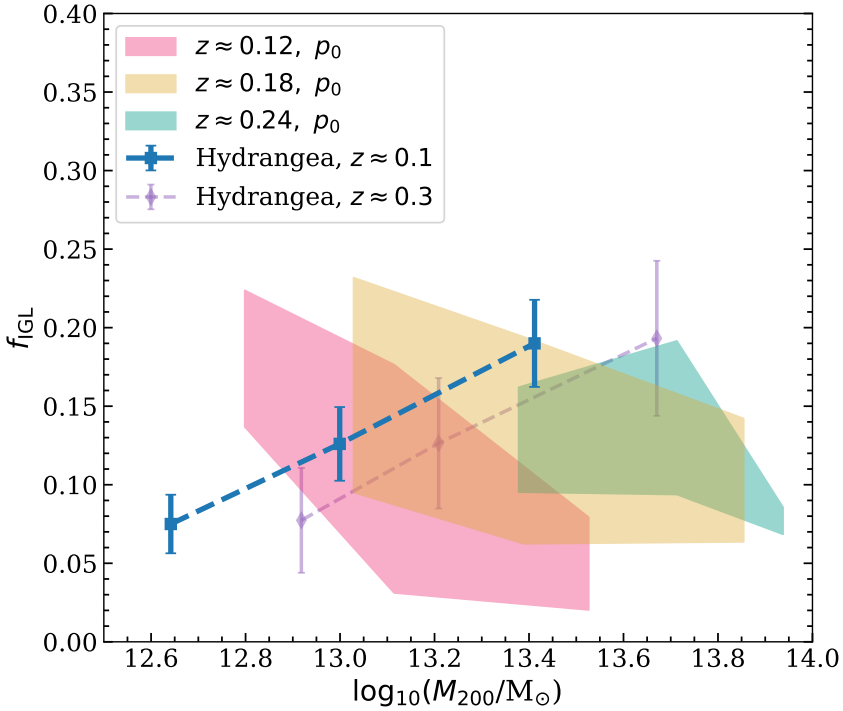

Figure 4.9: Fraction of light in IGL compared to the total group light ($f_{\rm IGL}$) of our KiDS+GAMA group sample at different redshifts from the 0^{th} order (p_0) background-subtracted images. The values along the x-axis indicate the mean halo mass M_h of the corresponding bins. Pink, yellow, and cyan shaded regions show the upper and lower limit of $f_{\rm IGL}$ for the redshift ranges $0.09 < z < 0.15$, $0.16 < z < 0.21$, and $0.21, z < 0.27$, respectively. Details on how we define the upper and lower limits for each of the measurements are discussed in the text. Blue and purple lines show the prediction of $f_{\rm IGL}$ measurement from Hydrangea simulations at comparable redshifts (mentioned in labels). The range of $f_{\rm IGL}$ is comparable between simulations and observations.

fainter at higher redshifts. As a result, we see a reduced over-subtraction compared to what we see in Fig. 4.8. As we measure faint and diffuse IGL, a naive initial assumption can be that the lower the redshift, the best measurement of the faint light we can get. However, after considering this background pattern issue, considering a slightly higher redshift bin can instead improve the robustness of the IGL measurement.

Comparison to other works

Our measurement of the IGL fraction is comparable to other existing IGL/ICL measurements. Given the halo mass range of our group sample, the strength of our measurements comes from stacking many groups, which reduced the scatter in our measurements compared to existing works, especially ones that are computed in individual systems. Martínez-Lombilla et al. (2023) measured the IGL fraction in a GAMA group with ID 4001389 (RA 35.834163 deg, DEC -5.454157; J2000) from the GAMA group catalogue G^3Cv10 (Robotham et al., 2011) using multi-band data from the Hyper Suprime-Cam Subaru Strategic Program Public Data Release 2 (Aihara et al., 2019). Their measurement of $f_{\rm IGL}$ using different surface brightness cuts and a 2D composite model spans 0.035 - 0.305 (among different methods) in the $r-$band. Although our method of separating CG from IGL is not the same one as they used, at the redshift ($z \approx 0.2$) and halo mass ($M_{\rm dyn} = 1.3 \times 10^{13} {\rm M}_{\odot}$) of their measured group, our measurements indicate $\sim 0.1 - 0.2$ for the p_0 images. In another recent work, Ragusa et al. (2023) measured IGL/ICL fractions for VST Early-type GAlaxy Survey (VEGAS, Iodice et al. 2021) data at $z \leq 0.05$, and their $f_{\rm IGL}$ measurements for individual groups at $M_{\rm vir} < 10^{14} {\rm M}_{\odot}$ ranges between ∼0.2 - 0.4 (from their fig. 2). Although their measurements are from the local Universe, unlike our slightly higher redshifts, we do not expect a lot of evolution on the IGL component over this time. Our measurements are also similar to the IGL fraction of individual groups at different redshifts from fig. 2 of Montes (2022), groups of different halo masses (using N-body simulations) from Rudick et al. (2011), and stacked measurements of 687 SDSS groups at $0.2 \leq z \leq 0.3$ from Zibetti et al. (2005). We found in Ahad et al. (2023) that the IGL fraction increases with the host halo mass and luminosity of the group CG. We do not see that trend in our KiDS+GAMA IGL measurements (as shown in Fig. 4.9). However, the range of values is comparable, and given the strong systematics in the background of our data, it is not possible to comment on the overall trend with certainty.

4.6 Discussion and Summary

Due to the small and large-scale background pattern in the KiDS data, even after our re-processing, it is quite challenging to obtain a clean measurement of the IGL. Nevertheless, using our custom background estimation and subtraction pipeline, careful selection and binning of sample groups, and stacking many groups to improve the SNR has allowed us to obtain a good constraint on the IGL measurement. This is the first well-constrained stacked measurement based on such a large sample of groups in the halo mass range we considered ($12.5 \leq \log_{10}[M_{200}/\mathrm{M}_{\odot}] \leq 14.0$). Moreover, this analysis highlights the potential of wide-field surveys for LSB analyses, such as the IGL measurement.

A crucial factor for robust IGL (or any LSB) measurement is a uniform and flat sky background with the minimum possible residual background pattern. Wide-field cameras, by construction, pick up light from a wide area of the sky in each field-of-view, and therefore particularly susceptible to stray light from passing objects outside of the field-of-view which cause internal reflection in the camera and non-uniform illumination patterns in the joined image. There can also be image regions that contain scattered light shadows from bond wire baffles. These issues need to be carefully resolved from pointings during the data processing stages. Along with these, there is one added layer of complexity that came with using KiDS data that overlap the GAMA fields-of-view. Because the GAMA overlapping regions were prioritized during the KiDS survey design, the data we used were taken in the early stages of the survey. These early data from KiDS suffered from a problem with the baffling, resulting in more stray light. The later data releases have these issues resolved, but the KiDS+GAMA fields were already in place by then. Therefore, instead of the GAMA overlapping fields, images from the later KiDS data production may be more suitable for LSB measurements once reprocessed by our custom pipeline with updated background subtraction. However, we lack a reliable group catalogue (like the GAMA catalogue we use here) in those regions.

Despite the challenging image data, with our carefully designed and tested analysis we present IGL measurement from the largest group sample so far, demonstrating the strength of a stacking analysis. Our complete pipeline (from data processing to sample selection and analysis steps) will be a useful tool for statistical analysis of the IGL across a wide halo-mass and redshift range for the next generation of wide-field surveys such as *Euclid* (Troja et al., 2023) and LSST (Ivezić et al., 2019).

4.6.1 Summary

Our main findings from this work are listed below.

- To optimize cosmology survey data for low-surface-brightness (LSB) analysis, the most important adjustment is to ensure a flat sky background. A non-uniform background can be caused by non-uniform illumination from reflections of stray light into the wide-field camera. On the data processing side, background patterns from over-subtraction of faint light around bright sources can be caused by local sky detection and subtraction based on small units of area on the large image. The issues caused by the instrument can be mostly modelled and corrected, and a new pipeline is needed to resolve the background subtraction issue. We perform these before our analysis.

- We tested the performance of different background estimation models in this work based on their effect on the scatter of mean background value at random points in the field-of-view (Fig. 4.3), and the retention of faint light in the extended galaxy profiles (Fig. 4.4). Based on these two criteria, we initially concluded that a first-order polynomial (p_1) for the background model had the most reasonable performance. However, the other two models (zeroth order, p_0, and second order, p_2) had their advantages too. Further analysis with images from all three cases showed that p_0 performs best in retaining the extended faint light for our brightest CG bins.

- We used our IGL measurement predictions based on cosmological simulations from Ahad et al. (2023), adjusted for the updated KiDS PSF, to compare with our results in this work. A comparison of the standard KiDS PSF and our updated image PSF shows improvement of faint light retention at the extended profile (Fig. 4.5). The effect of PSF convolution on the IGL fraction ($f_{\rm IGL}$) measurement is small, but non-negligible.

- Even after the updated background subtraction, there are residual large- and small-scale patterns in the background that affect the extended galaxy profiles where IGL dominates. Therefore it is necessary to compute and account for the residual background pattern at large radii for all the updated background-subtracted images.

- Not all the SB profiles of group central galaxies (CG) were usable for the stacked analysis due to the presence of significant irregularities which could potentially

bias the measurements. These irregularities were primarily caused by the presence of nearby bright sources or bad pixels due to random noise. All SB profiles were visually inspected and flagged for such irregularities. This conservative selection resulted in leaving about half of our initial group samples in the final measurement, but it made the measurement more reliable. Because of starting with a large sample, even after such a strict selection process, we had at least $\sim 250(\times 5$ exposures) groups in each redshift bin we considered.

- We obtained upper and lower limits for $f_{\rm IGL}$ for our group sample in the lowest redshift bin ($0.09 \leq z \leq 0.15$) from the three background-subtraction methods we used (Fig. 4.6). Due to over-subtraction of faint light at large radii, p_1 and p_2 models provide a lower limit to $f_{\rm IGL}$, while p_0 model provides an upper limit. Although the trend of $f_{\rm IGL}$ against the luminosity of group CGs from the KiDS+GAMA sample is not the same as predictions from simulations, the values are comparable.

- We repeated our analysis for two more consecutively higher redshift bins, with average group redshifts being $z \approx 0.18$ and $z \approx 0.24$ using the p_0 images to check for any redshift evolution in the measurement. The predictions from the simulations at $z = 0.3$ show a small sign of evolution. However, $f_{\rm IGL}$ from GAMA groups does not show a clear trend with redshift (Fig. 4.9). Overall, our measurements are consistent with existing works on systems with comparable halo mass and redshifts, and have a smaller scatter in the measurements because of stacking many groups.

- One interesting finding from analysis at higher redshifts is that stacked SB profiles at higher redshifts have reduced over-subtraction than at the lowest redshift bin, and therefore have a more reliable measurement. This is because the same physical size of groups corresponds to a smaller angular size at higher redshift. As a result, group cutouts with 1 Mpc side length span across fewer chips at higher redshifts, consequently avoiding large-scale residual background patterns in the image mosaic. This is especially prominent for the brightest CG bin (i.e. the most massive groups) at each redshift. Therefore, in this work, at the same average halo mass (or CG luminosity) of the stacked groups, measurements from a slightly higher redshift bin are more reliable than those at a lower redshift.

Acknowledgements

The authors acknowledge support from the Netherlands Organization for Scientific Research (NWO) under Vici grant number 639.043.512 (SLA, HH), and Veni grant number 639.041.751 (YMB). YMB also gratefully acknowledges financial support from the Swiss National Science Foundation (SNSF) under funding reference 200021_213076. The Hydrangea simulations were in part performed on the German federal maximum performance computer "HazelHen" at the maximum performance computing centre Stuttgart (HLRS), under project GCS-HYDA / ID 44067 financed through the large-scale project "Hydrangea" of the Gauss Center for Supercomputing. Further simulations were performed at the Max Planck Computing and Data Facility in Garching, Germany. This work used the DiRAC@Durham facility managed by the Institute for Computational Cosmology on behalf of the STFC DiRAC HPC Facility (www.dirac.ac.uk). The equipment was funded by BEIS capital funding via STFC capital grants ST/K00042X/1, ST/P002293/1, ST/R002371/1 and ST/S002502/1, Durham University and STFC operations grant ST/R000832/1. DiRAC is part of the National e-Infrastructure.

This research made use of data from the Galaxy and Mass Assembly survey (GAMA). GAMA is a joint European-Australasian project based around a spectroscopic campaign using the Anglo-Australian Telescope. The GAMA input catalogue is based on data taken from the Sloan Digital Sky Survey and the UKIRT Infrared Deep Sky Survey. Complementary imaging of the GAMA regions is being obtained by a number of independent survey programs including GALEX MIS, VST KiDS, VISTA VIKING, WISE, Herschel-ATLAS, GMRT, and ASKAP providing UV to radio coverage. GAMA is funded by the STFC (UK), the ARC (Australia), the AAO, and the participating institutions. The GAMA website is http://www.gama-survey.org.

The KiDS imaging data is based on observations made with ESO Telescopes at the La Silla Paranal Observatory under programme IDs 177.A-3016, 177.A-3017, 177.A-3018 and 179.A-2004, and on data products produced by the KiDS consortium. The KiDS production team acknowledges support from: Deutsche Forschungsgemeinschaft, ERC, NOVA and NWO-M grants; Target; the University of Padova, and the University Federico II (Naples).

The analysis of this work was done using Python (http://www.python.org), including the packages NumPy (Harris et al., 2020), AstroPy (Astropy Collaboration et al., 2013), and SciPy (Jones et al., 2009). Plots have been produced with Matplotlib (Hunter, 2007).

Data Availability

The data presented in the figures are available upon request from the corresponding author. The Hydrangea data are available at https://ftp.strw.leidenuniv.nl/bahe/Hydrangea/. The KiDS DR4 data are available at https://kids.strw.leidenuniv.nl/DR4/access.php, and the GAMA catalogues can be accessed from http://www.gama-survey.org/dr3/schema/.

References

Ahad, S. L., Bahé, Y. M., and Hoekstra, H., 2023, MNRAS, 518, 3685

Aihara, H., AlSayyad, Y., Ando, M., et al., 2019, Publications of the Astronomical Society of Japan, 71, 114

Alonso Asensio, I., Dalla Vecchia, C., Bahé, Y. M., et al., 2020, MNRAS, 494, 1859

Astropy Collaboration, Robitaille, T. P., Tollerud, E. J., et al., 2013, A&A, 558, A33

Bahé, Y. M. et al., 2017, MNRAS, 470, 4186

Barnes, D. J., Kay, S. T., Bahé, Y. M., et al., 2017, MNRAS, 471, 1088

Bertin, E. (July 2006). "Automatic Astrometric and Photometric Calibration with SCAMP". *Astronomical Data Analysis Software and Systems XV*. Ed. by C. Gabriel, C. Arviset, D. Ponz, et al. Vol. 351. Astronomical Society of the Pacific Conference Series, 112.

Bertin, E. and Arnouts, S., 1996, A&AS, 117, 393

Bertin, E., Mellier, Y., Radovich, M., et al. (Jan. 2002). "The TERAPIX Pipeline". *Astronomical Data Analysis Software and Systems XI*. Ed. by D. A. Bohlender, D. Durand, and T. H. Handley. Vol. 281. Astronomical Society of the Pacific Conference Series, 228.

Burger, P. A., Friedrich, O., Harnois-Déraps, J., et al., 2023, A&A, 669, A69

Capaccioli, M. and Schipani, P., 2011, The Messenger, 146, 2

Capaccioli, M, Schipani, P, De Paris, G, et al. (2012). *Science from the Next Generation Imaging and Spectroscopic Surveys*.

Contini, E. and Gu, Q., 2021, ApJ, 915, 106

Contini, E., 2021, Galaxies, 9, 60

Coogan, R. T., Daddi, E., Le Bail, A., et al., 2023, arXiv e-prints, arXiv:2302.08960

Crain, R. A., Schaye, J., Bower, R. G., et al., 2015, MNRAS, 450, 1937

de Jong, J. T. A., Verdoes Kleijn, G. A., Boxhoorn, D. R., et al., 2015, A&A, 582, A62

de Jong, J. T. A., Verdoes Kleijn, G. A., Erben, T., et al., 2017, A&A, 604, A134

DeMaio, T., Gonzalez, A. H., Zabludoff, A., et al., 2018, MNRAS, 474, 3009

DeMaio, T., Gonzalez, A. H., Zabludoff, A., et al., 2020, MNRAS, 491, 3751

Driver, S. P., Hill, D. T., Kelvin, L. S., et al., 2011, MNRAS, 413, 971

Driver, S. P., Norberg, P., Baldry, I. K., et al., 2009, Astronomy and Geophysics, 50, 5.12

Erben, T., Schirmer, M., Dietrich, J. P., et al., 2005, Astronomische Nachrichten, 326, 432

Furnell, K. E., Collins, C. A., Kelvin, L. S., et al., 2021, MNRAS, 502, 2419

Gaia Collaboration, Brown, A. G. A., Vallenari, A., et al., 2018, A&A, 616, A1

Gaia Collaboration, Brown, A. G. A., Vallenari, A., et al., 2021, A&A, 649, A1

Gallagher John S., I. and Ostriker, J. P., 1972, Astronomical Journal, 77, 288

Giblin, B., Heymans, C., Asgari, M., et al., 2021, A&A, 645, A105

Gonzalez, A. H., Sivanandam, S., Zabludoff, A. I., et al., 2013, ApJ, 778, 14

Guo, Q., White, S., Boylan-Kolchin, M., et al., 2011, MNRAS, 413, 101

Harris, C. R., Jarrod Millman, K., van der Walt, S. J., et al., 2020, arXiv e-prints, arXiv:2006.10256

Hunter, J. D., 2007, Computing in science & engineering, 9, 90

Iodice, E., Spavone, M., Capaccioli, M., et al., 2021, The Messenger, 183, 25

Ivezić, Ž., Kahn, S. M., Tyson, J. A., et al., 2019, ApJ, 873, 111

Jakobs, A., Viola, M., McCarthy, I., et al., 2018, MNRAS, 480, 3338
Jiménez-Teja, Y., Dupke, R., Benítez, N., et al., 2018, ApJ, 857, 79
Jones, D. H., Read, M. A., Saunders, W., et al., 2009, MNRAS, 399, 683
De Jong, J. T. A., Kuijken, K., Applegate, D., et al., 2013, The Messenger, 154, 44
Joo, H. and Jee, M. J., 2023, Nat., 613, 37
Kluge, M., Bender, R., Riffeser, A., et al., 2021, ApJS, 252, 27
Kuijken, K., 2011, The Messenger, 146, 8
Kuijken, K., Heymans, C., Dvornik, A., et al., 2019, A&A, 625, A2
Li, S.-S., Hoekstra, H., Kuijken, K., et al., 2023, arXiv e-prints, arXiv:2306.11124
Liske, J., Baldry, I. K., Driver, S. P., et al., 2015, MNRAS, 452, 2087
Lotz, J. M., Koekemoer, A., Coe, D., et al., 2017, ApJ, 837, 97
Martínez-Lombilla, C., Brough, S., Montes, M., et al., 2023, MNRAS, 518, 1195
McFarland, J. P., Verdoes-Kleijn, G., Sikkema, G., et al., 2013, Experimental Astronomy, 35, 45
Mihos, C. (Aug. 2015). "Intragroup and Intracluster Light". *IAU General Assembly*. Vol. 29, 2247903, 2247903.
Mihos, J. C., Harding, P., Feldmeier, J., et al., 2005, ApJL, 631, L41
Mihos, J. C., Harding, P., Feldmeier, J. J., et al., 2017, ApJ, 834, 16
Montes, M., 2022, Nature Astronomy, 6, 308
Montes, M., Brough, S., Owers, M. S., et al., 2021, ApJ, 910, 45
Montes, M. and Trujillo, I., 2014, ApJ, 794, 137
Montes, M. and Trujillo, I., 2018, MNRAS, 474, 917
Montes, M. and Trujillo, I., 2019, MNRAS, 482, 2838
Murante, G., Giovalli, M., Gerhard, O., et al., 2007, MNRAS, 377, 2
Puchwein, E., Springel, V., Sijacki, D., et al., 2010, MNRAS, 406, 936
Ragusa, R., Iodice, E., Spavone, M., et al., 2023, A&A, 670, L20
Robotham, A. S. G., Norberg, P., Driver, S. P., et al., 2011, MNRAS, 416, 2640
Rudick, C. S., Mihos, J. C., and McBride, C. K., 2011, ApJ, 732, 48
Schaller, M., Dalla Vecchia, C., Schaye, J., et al., 2015, MNRAS, 454, 2277
Schaye, J., Crain, R. A., Bower, R. G., et al., 2015, MNRAS, 446, 521
Schirmer, M., 2013, ApJS, 209, 21
Steinhardt, C. L., Jauzac, M., Acebron, A., et al., 2020, ApJS, 247, 64
Taylor, E. N., Hopkins, A. M., Baldry, I. K., et al., 2011, MNRAS, 418, 1587
Tonnesen, S. and Bryan, G. L., 2012, MNRAS, 422, 1609
Troja, A., Tutusaus, I., Sorce, J., et al. (June 2023). "Euclid in a nutshell". *41st International Conference on High Energy physics*, 94, 94. DOI: 10.48550/arXiv.2211.09668. arXiv: 2211.09668 [astro-ph.IM].
Viola, M., Cacciato, M., Brouwer, M., et al., 2015, MNRAS, 452, 3529
Werner, S. V., Hatch, N. A., Matharu, J., et al., 2023, MNRAS, 523, 91
Wright, A. H., Robotham, A. S. G., Bourne, N., et al., 2016, MNRAS, 460, 765
Zhang, Y., Yanny, B., Palmese, A., et al., 2019, ApJ, 874, 165
Zibetti, S., White, S. D. M., Schneider, D. P., et al., 2005, MNRAS, 358, 949

Appendix A

Test with different mask extensions

The fraction of unmasked diffuse light around sources other than the CG is expected to decrease with increasing redshift, because at higher redshifts the faint signals are likely to be comparable to the background noise level. Therefore, we tested the effect of an extended masking on removing the diffuse light from satellites for the subsample

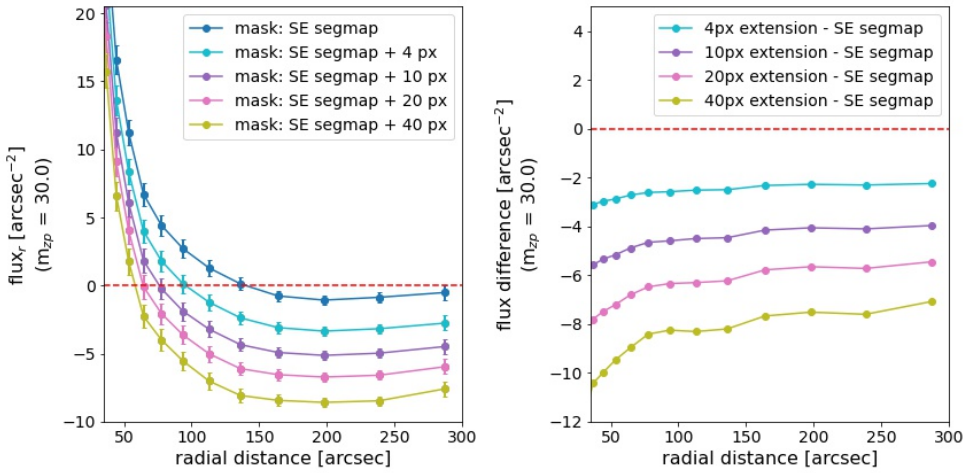

Figure 4.A.1: Left: surface brightness (SB) profiles of group central galaxies (CG) beyond 50" with different levels of mask-extension (as shown in the top-right corner). Compared to the original segmentation map (blue), the 4, 10, 20, and 40-pixel extended masks to sources other than CG produce monotonically lower flux profiles. Error bars show the 1 σ error to the corresponding mean values. Right: change of measured SB profiles of the stacked BGGs. Different lines here show the difference between different levels of mask extension (as shown in the top-right corner) compared to the initial mask obtained from the segmentation map of SExtractor . The main noticeable feature from both the panels is that, even with a 4-pixel (about 1.3 kpc) extension to the segmentation map, the outer profile is lowered by about 3 ADU compared to the original mask from the segmentation map.

of GAMA groups at the lowest redshift bin, which is at $0.09 < z < 0.15$. We picked the groups with the brightest BGGs ($M_r < -23$) in this lowest z bin for this test to have comparable light profiles for the stacking. The masks for the sources obtained from the segmentation map were extended by 4, 10, 20, and 40 pixels by convolving them with a two-dimensional box kernel of the corresponding pixel size, and these extended masks were added to the already existing masks of the bright stars and bad columns as explained in Sec. 4.2.3. The fluxes from the unmasked pixels were then used to estimate radial surface brightness (SB) profiles of individual group images and then stacked together to obtain the final SB profiles for the different mask extension levels, including the original mask without any extension.

A comparison of the SB profiles with the original mask from the segmentation maps and different extended masks is shown in Fig. 4.A.1. The left panel shows a zoomed-in plot of the SB profiles at larger radii for all the mask levels. The expected noticeable point is that compared to the original segmentation map (blue), the 4 (cyan), 10

(purple), 20 (pink), and 40 (olive) pixels extended masks produced monotonically lower flux profiles. This implies that an extended mask indeed results in retaining a lower SB profile. The right panel of Fig. 4.A.1 shows the change of measured radial surface brightness profiles of the stacked BGGs. The different lines show the difference of the CG SB profile for different levels of mask extension (as shown in the labels) compared to the initial mask obtained from the segmentation map of SExtractor (labelled as 'SE segmap'). From the group centre out to 20 arcseconds, the difference is negligible because the CG is unmasked (not shown here). Beyond 20", the increasing mask extension resulted in increasingly lower flux values.

An interesting feature from the right panel is that beyond 100", the profile differences are slightly different from each other. The original segmentation map and 4 pixels-extended masks produced similar SB profiles, resulting in a smooth outer profile for the difference in these cases (cyan line in the right panel). However, the 10, 20, and 40 pixels-extended masks produced slightly different outer SB profiles, resulting in a slightly uneven pattern in the outer profiles in the right panel. This is likely because there is still some extended light from satellites left in the original segmentation map and with 4-pixel mask extensions, which is covered for 10-pixel and larger mask extensions. It implies that a minimum of 10 pixels mask extension is needed to remove the extended light from the satellite galaxies contributing to the uneven light profile. The similar profiles between 10, 20, and 40-pixel extension implies that the removal of uneven light does not improve between these extension levels. Moreover, in the left panel, it is visible that with increased mask extensions, there is increased over-subtraction of faint light, resulting in negative values in the SB profiles beyond 50 kpcs.

To sum up, we found that masks from the original segmentation map and the 4-pixel extension are too small to exclude residual extended light from satellites. At the same time, a larger (20 or 40 pixels) extension of the segmentation map over-subtracts the extended light. Considering both issues, we decided to use a 10-pixel extension to the original segmentation map as our default mask size.